Nanostructures

International Edition: DOI: 10.1002/anie.201411685
German Edition: DOI: 10.1002/ange.201411685

Synthesis of Nanostructured Carbon through Ionothermal Carbonization of Common Organic Solvents and Solutions**

*Yuanqin Chang, Markus Antonietti, and Tim-Patrick Fellinger**

Abstract: *A combination of ionothermal synthesis and hot-injection techniques leads to novel nanocarbons made from organic solvents. Controlled addition of commonly used organic solvents into a hot $ZnCl_2$ melt gives rise to spherical, sheetlike, and branched nanofibrous carbon nanoparticles with surprisingly high carbon efficiency. When heteroatom-containing solvents were used, the doping levels reach up to 14 wt.% nitrogen and 13 wt.% sulfur. Materials with high surface areas and large pore volumes of solvent carbons as high as 1666 $m^2 g^{-1}$ and 2.80 $cm^3 g^{-1}$ in addition to CO_2 adsorption capacities of 4.13 $mmol g^{-1}$ at 273 K and 1 bar can be obtained. The new method works not only for pure carbon materials, but was also extended for the synthesis of carbon/inorganic nanocomposites. ZnS@C, Ni@C, and Co@C were successfully prepared with this straightforward procedure. The obtained Ni@C nanocomposites perform well in the electrocatalytic water oxidation, comparable with commercial noble-metal catalysts.*

Carbon(aceous) nanomaterials, due to their unique physical and chemical properties, including electric conductivity, chemical stability, and unique morphology (high surface area and porosity), are an important class of materials with a large number of applications including adsorption, separation, and energy conversion and storage.[1] Typically carbon nanomaterials are synthesized in bulk processes. Because carbonization requires high-temperature pyrolysis conditions, precursors with low volatility are used. Bulk processes and solid-state transformations, however, always have the disadvantage of restricted mass transport and low reorganizational dynamics so that mainly disordered as well as heterogeneous products are obtained. This can be improved by carbon synthesis from the gas phase, and not only fullerenes,[2] nanotubes,[3] and graphenes,[4] but also colloidal carbon species such as printing inks and conduction soots can be made.[5] However, also gas-phase processes have their specific disadvantages, mainly low space–time yields, and poor heat transfer and temperature control.

A "wet-chemical" route to carbon materials under pyrolysis conditions could solve many of the abovementioned problems, and most nanomaterials other than carbons, such as metal or metal chalcogenide nanoparticles (NPs), can usually be synthesized using nucleation and growth mechanisms,[6] for example, via hot-injection techniques.[7] The resulting nanostructures can be transformed into carbon; in the first step the desired morphology is realized from organic precursors (via for example, resorcinol formaldehyde resin polymerization[8] or hydrothermal carbonization[9]), followed by pyrolysis in a second step.

Typical carbonizable polymers include poly(acrylonitrile),[10] resorcinol formaldehyde resin,[8] poly(furfuryl alcohol),[11] and poly(aniline),[12] as well as natural products like chitosan[13] and cellulose.[14] The main drawback here is that the final carbon structures undergo significant shrinkage due to mass loss and their high surface energy.[15] Therefore, an ideal solution-phase technique should create the desired and stable carbon nanostructures in one step directly.

Recently we reported on a novel "wet-chemical" synthesis route using inorganic salt melts as solvents for the synthesis of high-surface-area and aerogel-like nanocarbons.[16] The inorganic salt melts or fluxes act first as solvents and later as porogens throughout the condensation temperatures, where the carbonaceous material mechanically stabilizes against shrinkage. The resulting carbons can be easily isolated when the cold reaction mixtures are washed with water. Viable precursors need to be: 1) thermally stable and not evaporating up to the melting point of the inorganic salt solvent; 2) miscible with or soluble in the salt melt, and 3) carbonizable. So far this could only be realized using task-specific ionic liquids[17] and glucose.[18]

In order to synthesize carbon nanomaterials even more conveniently and economically, we introduce herein a salt-melt-based ionothermal carbonization via hot injection. Due to the very fast pyrolytic monomer decomposition step, a selection of ten commonly used, highly volatile but cheap organic solvents could be used as carbon precursors in a high-temperature (up to 550 °C) Schlenck-type reactor using molten $ZnCl_2$ as a solvent (Scheme 1). All organic solvents were successfully converted into carbonaceous nanomaterials in sometimes surprisingly high yields. Depending on the actual precursor, the solvent nanocarbons are heteroatom doped and show high surface areas (SAs), pore volumes, and CO_2 adsorption capacities. More interestingly, three different characteristic morphologies were obtained depending on the composition and chemical properties of the solvent precursor. This method was further employed for the one-step synthesis of carbon/inorganic nanocomposites, which in one example show superior activity in the electrocatalytic water oxidation.

[*] Dr. Y. Chang, Prof. Dr. M. Antonietti, Dr. T.-P. Fellinger
Max-Planck-Institut für Kolloid- und Grenzflächenforschung
Am Mühlenberg 1, 14476 Potsdam (Germany)
E-mail: Tim.Fellinger@mpikg.mpg.de

[**] We thank the members of the research group Carbon and Energy/MPIKG for useful discussions, Sören Selve (TU Berlin) for HRTEM measurements, and Fei Hong (Shenzhen University, China) for XPS measurements.

Supporting information for this article is available on the WWW under http://dx.doi.org/10.1002/anie.201411685.

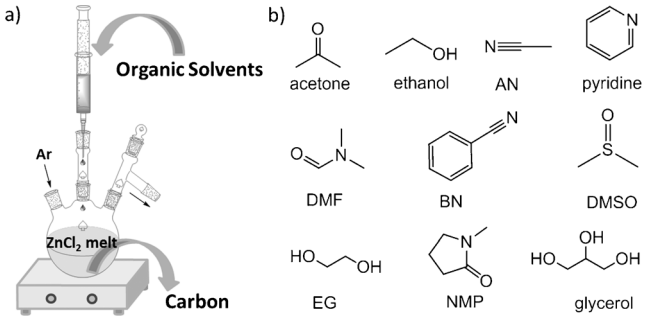

Scheme 1. a) Schematic illustration of solvent-injection carbonization setup; b) molecular structures of the solvents.

Solvent injection carbonization requires a high-temperature Schlenck line and typical glassware for organic synthesis including Duran flasks (Scheme 1a and the Supporting Information). Equal volumes of solvent (2 mL) were injected into a $ZnCl_2$ melt at a constant rate using a syringe pump under argon flow. The herein presented carbonaceous nanomaterials were directly derived from acetone, ethanol, acetonitrile (AN), pyridine, dimethyl formamide (DMF), benzonitrile (BN), dimethylsulfoxide (DMSO), ethylene glycol (EG), *N*-methylpyrrolidone (NMP), and glycerol (Scheme 1b). The products were obtained in yields between 4.1% for pyridine and 37.5% for NMP, and the products could be easily collected after washing with hydrochloric acid and vacuum drying at 60°C for 8 h. For convenience, the respective carbonaceous products will be denoted as "solvent name/abbreviation"-C in the following.

Scanning electron microscopy (SEM) imaging was performed to gain insight into the different solvent carbon morphologies (Figure 1a, Figure S1 in the Supporting Information). Interestingly, the conversion of the ten solvents gives rise to three different prominent product morphologies. AN-C, BN-C, and DMSO-C mostly show aggregates of spherical primary NPs. This morphology is similar to that of polycondensation-based carbonaceous materials, such as the classical resorcinol-formaldehyde- or borax-mediated hydrothermal carbon, the abovementioned ionic-liquid-based carbon,[9,19] and carbons prepared by gas-phase processes. The second characteristic morphology is sheets, which are obtained for EG-C and Glycerol-C. Similar sheetlike structures were recently also obtained in our group through the pyrolysis of glucose in a LiCl/KCl mixture. However, these even thinner, few-layer graphenes are very likely formed by a different mechanism.[18]

A more complicated third structure was observed for ethanol-C, acetone-C, pyridine-C, DMF-C, and NMP-C. These nanocarbons manifest an interconnected branched, nanofibrous morphology. It has to be mentioned that the different morphologies were only obtained in the case of liquid injection, whereas carbonization of vapors (which is also possible) usually leads to nanospheres (Figure S2). Transition electron microscopy (TEM) imaging was per-

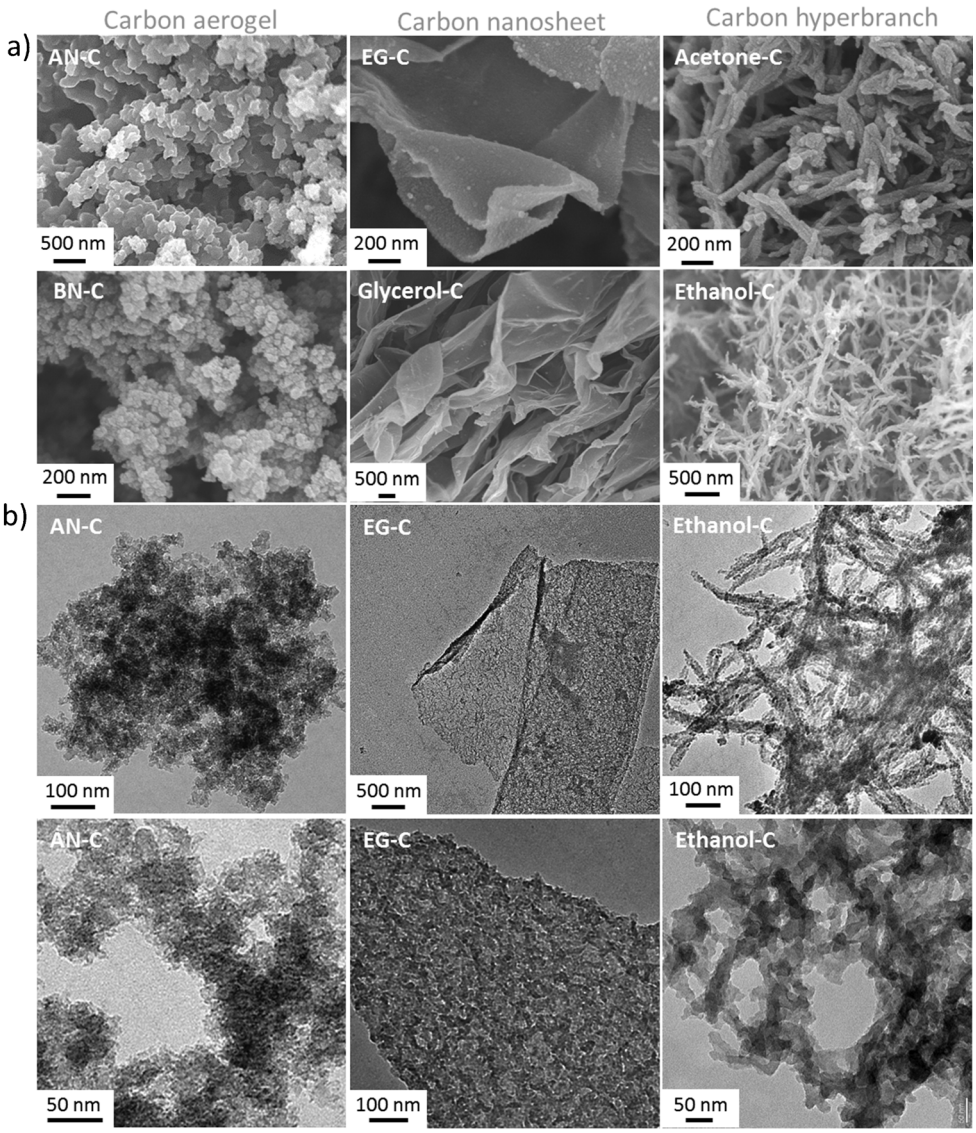

Figure 1. a) SEM images of representative solvent carbons. b) TEM images of representative solvent carbons.

formed to further study the architecture of the different solvent nanocarbons (AN-C for the nanospheres, EG-C for the nanosheets, and ethanol-C for the branched nanofibers; Figure 1b). In the case of AN-C, the spherical particles are roughly 10 nm in diameter. Interstitial gaps between the particles lead to an open meso- and macroscopic pore system. The second morphology, wrinkled nanosheets like that seen for EG-C, shows sheets many micrometers across and with a thickness of about 100 nm. The sheets are highly porous/nanostructured and have a homogeneous appearance with pores apparently in the mesopore range. For ethanol-C the characteristic branched nanofibers are composed of similar, but anisotropic NPs mutually aligned to give an interesting fibrous morphology. The branches are several hundreds of nanometers in length and about 120 nm in width. The fibers' aspect ratio increases in the order of NMP-C < DMF-C < pyridine-C < acetone-C < ethanol-C and reaches a maximum value of ca. 10 in molten $ZnCl_2$. The fibers are randomly branched by nonlinear defect aggregation, leading overall to an open porous scaffold, again with interstitial pores on the meso- and macroscale.

Since we used a variety of organic solvents with different chemical features and obtained only three morphologies, it is interesting to speculate about the mechanisms of generation. Compounds containing a nitrile group (AN and BN), which can undergo fast pericyclic reactions, or easily decomposing compounds like DMSO will carbonize instantly to give spherical NPs without anisometry and inner order by simple growth of the nuclei. The aggregation of these structures consequently gives "ordinary" carbon aerogels, as found many times before. Vectorial alignment towards supramolecular assemblies such as nanorods and sheets was previously not known for carbon nanostructures, but is well established for inorganic NPs.[21] Here, the Hamaker interactions (force fields) between NPs are anisotropic due to different polarization tensors within the primary particles, and nanorods as well as nanosheets are usually obtained. For carbon NPs, this type of anisotropy could result from a corresponding preferred orientation of, for example, graphene sheets within the particle; that is, a slight preference of a cylindrical orientation would lead to one polarization direction, and a more sheetlike inner structure would lead to two polarization directions. In our carbons the structural arrangement is allowed due to mobility as an added value of the salt flux. In our opinion this nicely explains the aggregate morphologies observed. Of course, the quality of alignment will depend on the quality of the orientation within the primary particles and the mobility of the system, which in turn will depend on the reaction medium and the reaction conditions. To further investigate this factor in a simple proof-of-concept experiment, we employed a much less viscous 3:1 $LiCl/ZnCl_2$ mixture to synthesize NMP-based carbon. NMP-C prepared in pure $ZnCl_2$ has a branch length of 100 nm. However, the preparation in the $LiCl/ZnCl_2$ melt generated NMP-C with a more than tenfold increased branch length, that is, an aspect ratio of roughly 50 (Figure S3a). A stereoscopic view obtained from tilt-angle HRTEM images of NMP-C from the $LiCl/ZnCl_2$ melt as a preliminary result (Figure S3b) indicates that the nanofibers are indeed formed by primary graphenes assembled in parallel to the fiber vector. Interestingly, this orientation of theprimary graphene sheets within the NPs does not compromise their ability to form micropores, as some of the samples with high alignment still show rather high SAs (see sample Ethanol-C).

Nitrogen sorption analysis was carried out to further examine and quantify the porosity of the solvent nanocarbons (Figure S4). The BET SAs and total pore volumes can reach impressive values; however, they dramatically vary according to the chosen precursors. Interestingly, the SA does not correlate with the morphology, suggesting that local chemical properties, such as the interaction with the salt define mainly the molecular addition schemes and thereby the overall microporosity. Ethanol-C, AN-C, and DMSO-C after simple vacuum-drying have very high SAs of 1621, 1666, and 1387 $m^2 g^{-1}$ and large total pore volumes of 2.80, 2.69, and 2.30 $cm^3 g^{-1}$ (Figure 2a). Other precursors, including EG, glycerol, NMP, BN, and pyridine still result in relatively high SAs above 400 $m^2 g^{-1}$. The pore size distribution (Figure S5) additionally verifies hierarchical porosity, in which interstitial voids between the microporous aggregated particles form an open pore system.

The solvent nanocarbons show an interesting combination of properties—high heteroatom content, very high porosity, and a large proportion of very small micropores—which make them good candidates for CO_2 adsorption. Experimentally, AN-C and Ethanol-C with very high sorption capacities of

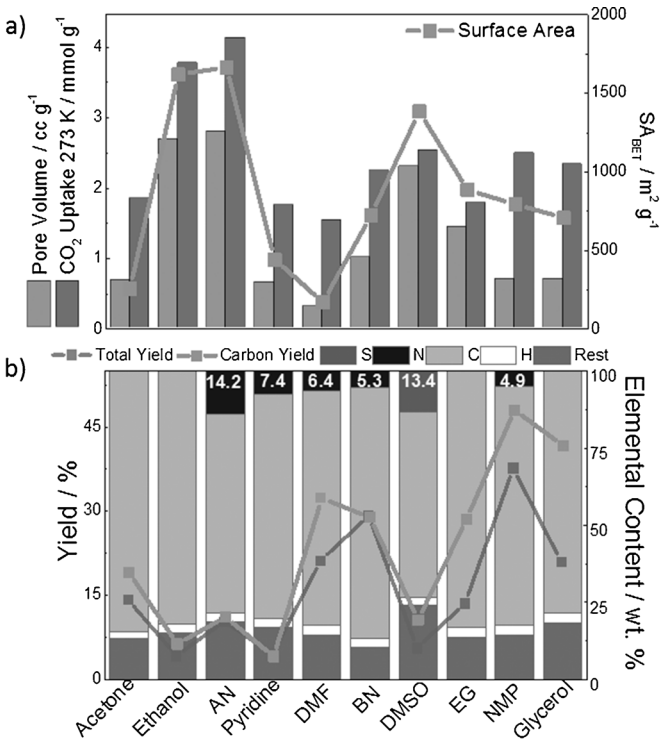

Figure 2. a) Gas sorption capacities of solvent carbons. b) Total yield, carbon yield, and elemental composition of solvent carbons. The total yield was determined from the mass ratio of the solvent carbon and the solvent used. The carbon yield was calculated form the total yield multiplied by the carbon yield and divided by the carbon content of the solvent.

4.13 and 3.77 mmol g^{-1} outperformed widely used commercial microporous carbon black (Black Pearl 2000, BET SA 2000 $m^2 g^{-1}$), and are comparable to some metal organic framework (MOF) materials (Figure S6).[22] A summary of the gas sorption data can be found in Figure 2a. We can observe a correlation of BET SA and CO_2 sorption, which indicates that the high CO_2 capacity is more due to physisorption in suitable pores than chemisorption in the bulk of the material.

The carbon yield can be regarded as an indicator of the condensation efficiency, and this yield is highly dependent on the actual precursor. Note that solvents with very low carbonization efficiencies are not necessarily undesired. Solutions prepared from such solvents can be used for the injection of nonliquid precursors without causing much structural contamination in the final product. AN-C shows the highest SA and pore volume, but is condensed to solids only with about 10% carbon atom efficiency. In contrast, EG and NMP can be converted into carbons with high SAs of 886 and 795 $m^2 g^{-1}$ with good efficiency and carbon yields of roughly 40 and 60% C, respectively. Another very interesting observation is that the polyol solvents undergo a very high degree of carbonization, with C contents of around 80%, indicating the loss of most of the hydroxy functions, which is similar to the case when glucose was used as the precursor.[18] A summary of the yields and chemical compositions of all solvent nanocarbons is shown in Figure 2b.

Total yields and carbon atom efficiencies indicate a strong interaction between the organic solvent and the salt melt that counteracts simple evaporation. A qualitative proof of this interaction can be obtained from thermogravimetric analysis (TGA) and differential scanning calorimetry (DSC) (Figures S7 and S8) of a simple mixture of solvent and $ZnCl_2$, indicating that the evaporation of the solvents was dramatically suppressed by the presence of $ZnCl_2$.

Another important property of carbons/carbonaceous materials is the heteroatom content, which can dramatically influence the product properties. Elemental analysis data show that AN-C, pyridine-C, DMF-C, BN-C, and NMP-C are nitrogen doped with up to 14 wt.% in the case of AN-C. DMSO-C is highly sulfur doped, with a sulfur content of 13.4 wt.%. Residual masses increase with increasing SA, indicating oxygen-containing functional groups. Fourier transform infrared (FTIR) spectroscopy (Figure S9) was used to investigate the heteroatom functionalization of the solvent nanocarbons. Typical C=N and C=S vibrations can be observed for the respective N-doped and S-doped carbons. The rather low intensity of the OH vibrations for materials from the alcoholic precursors underlines the aforementioned high degree of water elimination. X-ray photoelectron

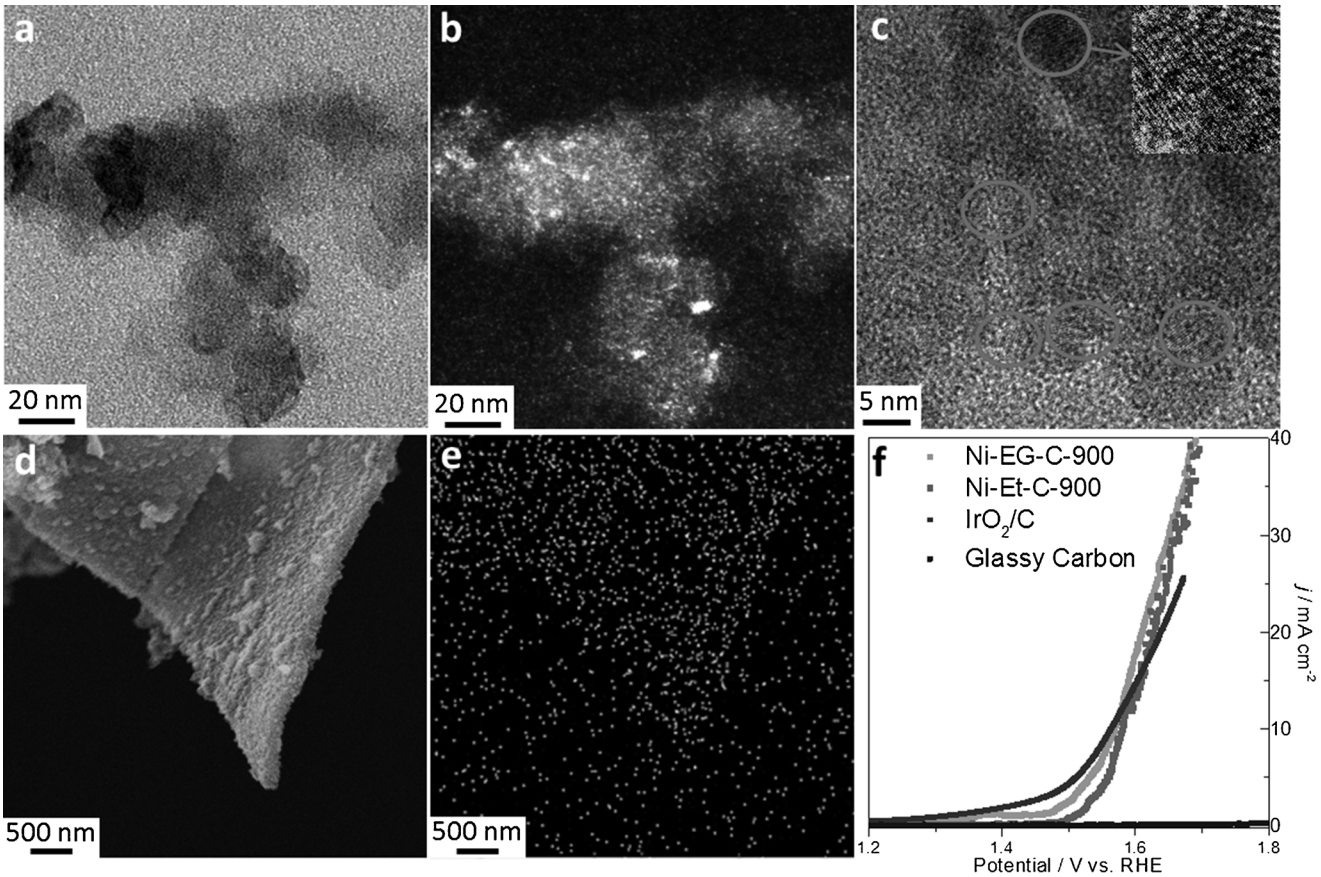

Figure 3. a) TEM, b) dark-field TEM and c) HR-TEM image of ZnS-DMSO-C. d) SEM image of Ni-EG-C. e) EDX Kα imaging of nickel in Ni-EG-C; f) OER performance of Ni@C composites and IrO_2/C in 0.1 M KOH.

spectroscopy (XPS) verifies the existence of pyridinic-N and graphitic-N atoms for all N-containing carbons. The S2p spectra indicate oxidized S species. The high-resolution spectra as well as quantification of the single sites can be found in the Supporting Information (Figure S10).[23]

The degree of carbonization was further investigated by Raman spectroscopy and X-ray diffraction (XRD) (Figure S11). Here we can observe that, even at a relatively low temperature of 550 °C, all solvent carbons show well-defined characteristic D and G bands with relatively high intensity ratio of G and D.[24] This observation is very promising for the low-temperature synthesis of graphitic materials.

Carbon-supported inorganic nanocomposites in some cases such as Ni/N/C[25] show synergistic property enhancements compared to the properties of single compounds and can serve, for example, as high-performance electrocatalysts.[1d,26] To underline the versatility and scope of the herein presented methodology beyond the synthesis of pure carbons, the ionothermal hot-injection technique was further extended to the preparation of carbon/inorganic nanocomposites.

In the first example, KOH is used instead of HCl for the postsynthetic purification of DMSO-C, which resulted in a ZnS/DMSO-C nanocomposite. HRTEM investigation and dark-field imaging reveals the ZnS nanocrystals to be approximately 15 nm in diameter, which is in good agreement with the average particles size of about 17 nm determined from XRD by means of the Debye–Scherrer equation (Figure S12a). The particles are homogeneously embedded into the retained DMSO-C aerogel morphology, and grain boundaries between different ZnS particles can be clearly observed (Figure 3 a–c). The ZnS crystals are directly formed from the pyrolytic decomposition products of DMSO. In other examples simple organic solutions of nickel acetate and nitrate in EG and ethanol (1.7 and 2.5 wt.% Ni solutions, respectively) were used as the injection precursor for the synthesis of Ni@C nanocomposites (denoted as Ni-EG-C and Ni-Et-C). For the composite materials, a homogeneous distribution of nickel atoms on the carbon was proven by TEM and energy-dispersive X-ray spectroscopy (EDX) while the morphology is the same as that of the original solvent carbon (Figure 3 d,e, Figures S13 and S14). X-ray diffractograms of Ni-based composites reveal a Ni^0 phase (JCPDS No. 87-712) due to carbothermal reduction (Figure S12b) with a calculated particle size of approximately 30 nm. Postsynthetic thermal treatment at 900 °C under inert atmosphere was carried out to increase the conductivity for electrochemical measurements. It should be mentioned that all solvent carbons can be treated thermally without losing the characteristic nanomorphology (Figure S15).

The electrocatalytic properties of the nickel nanocomposites were tested towards oxygen evolution in O_2-saturated 0.1 M KOH. The overpotential at 10 mA cm^2 was used to evaluate the activity.[27] For Ni-EG-C-900 and Ni-Et-C-900 the overpotentials are 339 and 350 mV, respectively, while the expensive commercial noble-metal-based water oxidation catalyst (IrO_2/C) has an overpotential of 334 mV at the same current density (Figure 3 f, Figure S16 for Tafel plots). At higher current density, the overpotentials of Ni@C are even lower than those of IrO_2/C.

$Co(OH)_2$-DMF-C was also synthesized by using a solution of cobalt acetate in DMF (3.1 wt.% Co) as the carbon source. The material showed a characteristic diffraction pattern of the $Co(OH)_2$ phase (JCPDS No. 30-443, Figure S12c). Postsynthetic thermal treatment at 900 °C reduced the $Co(OH)_2$ to Co^0 (JCPDS No. 15-806). Co-DMF-C-900 (as well as AN-C-900) was employed as an oxygen reduction catalyst in alkaline solution with an onset potential of 0.84 V vs. RHE, and showed much higher activity than the Co-free DMF-C-900 (Figure S17).

In summary, a variety of carbon nanomaterials with different morphologies, including aggregated nanospheres, nanosheets, and branched nanofibrous structures, were obtained by hot-injection carbonization of common organic solvents into a $ZnCl_2$ salt melt. Considering the ready availability of the solvents and the ease of synthesis, the carbon yields are competitive among other carbon nanomaterials syntheses. Furthermore, the whole synthesis requires only ordinary glassware and can be scaled up readily. When heteroatom-containing solvents are used as the carbon source, heteroatom-doped carbon products with up to 14 wt.% nitrogen and 13 wt.% sulfur could be obtained with high specific SAs, high pore volumes, and impressive CO_2 adsorption capacities at the same time. Additionally, the method was further applied for the synthesis of carbon/inorganic nanocomposites, such as ZnS@DMSO-C, Ni@C, and Co@C nanocomposites. The latter was shown to have interesting electrochemical performance. Given the tremendous number of combinations of inorganic salts and organic solvents, this approach has the potential for the designed synthesis of task-specific, customized hybrid materials, useful for applications in heterogeneous catalysis and in energy conversion and storage.

Keywords: carbon nanostructures · composite materials · electrocatalysts · hot injection · ionothermal synthesis

How to cite: *Angew. Chem. Int. Ed.* **2015**, *54*, 5507–5512
Angew. Chem. **2015**, *127*, 5598–5603

[1] a) S. Sircar, T. C. Golden, M. B. Rao, *Carbon* **1996**, *34*, 1–12; b) R. Ryoo, S. H. Joo, M. Kruk, M. Jaroniec, *Adv. Mater.* **2001**, *13*, 677–681; c) L. Dai, D. W. Chang, J.-B. Baek, W. Lu, *Small* **2012**, *8*, 1130–1166; d) Y. Liang, Y. Li, H. Wang, H. Dai, *J. Am. Chem. Soc.* **2013**, *135*, 2013–2036.
[2] S. Iijima, *Nature* **1991**, *354*, 56–58.
[3] P. Ajayan, *Chem. Rev.* **1999**, *99*, 1787–1800.
[4] a) A. Reina, X. Jia, J. Ho, D. Nezich, H. Son, V. Bulovic, M. S. Dresselhaus, J. Kong, *Nano Lett.* **2009**, *9*, 30–35; b) X. Li, C. W. Magnuson, A. Venugopal, R. M. Tromp, J. B. Hannon, E. M. Vogel, L. Colombo, R. S. Ruoff, *J. Am. Chem. Soc.* **2011**, *133*, 2816–2819.
[5] M. Voll, P. Kleinschmit, *Ullmann's Encyclopedia of Industrial Chemistry*, Wiley-VCH, Weinheim, **2010**.
[6] V. K. LaMer, R. H. Dinegar, *J. Am. Chem. Soc.* **1950**, *72*, 4847–4854.
[7] S. G. Kwon, T. Hyeon, *Acc. Chem. Res.* **2008**, *41*, 1696–1709.
[8] J. Liu, S. Z. Qiao, H. Liu, J. Chen, A. Orpe, D. Zhao, G. Q. Lu, *Angew. Chem. Int. Ed.* **2011**, *50*, 5947–5951; *Angew. Chem.* **2011**, *123*, 6069–6073.
[9] T. P. Fellinger, R. J. White, M. M. Titirici, M. Antonietti, *Adv. Funct. Mater.* **2012**, *22*, 3254–3260.

[10] Y. Chang, F. Hong, C. He, Q. Zhang, J. Liu, *Adv. Mater.* **2013**, *25*, 4794 – 4799.
[11] S. H. Joo, S. J. Choi, I. Oh, J. Kwak, Z. Liu, O. Terasaki, R. Ryoo, *Nature* **2001**, *412*, 169 – 172.
[12] G. Wu, K. L. More, C. M. Johnston, P. Zelenay, *Science* **2011**, *332*, 443 – 447.
[13] Y. Yang, J. Cui, M. Zheng, C. Hu, S. Tan, Y. Xiao, Q. Yang, Y. Liu, *Chem. Commun.* **2012**, *48*, 380 – 382.
[14] M. Sevilla, A. B. Fuertes, *Carbon* **2009**, *47*, 2281 – 2289.
[15] J. S. Lee, X. Wang, H. Luo, S. Dai, *Adv. Mater.* **2010**, *22*, 1004 – 1007.
[16] N. Fechler, T. P. Fellinger, M. Antonietti, *Adv. Mater.* **2013**, *25*, 75 – 79.
[17] K. Elumeeva, N. Fechler, T. Fellinger, M. Antonietti, *Mater. Horiz.* **2014**, *1*, 588 – 594.
[18] X. Liu, C. Giordano, M. Antonietti, *Small* **2014**, *10*, 193 – 200.
[19] A. M. ElKhatat, S. A. Al-Muhtaseb, *Adv. Mater.* **2011**, *23*, 2887 – 2903.
[20] a) P. F. Zhang, J. Y. Yuan, T. P. Fellinger, M. Antonietti, H. R. Li, Y. Wang, *Angew. Chem. Int. Ed.* **2013**, *52*, 6028 – 6032; *Angew. Chem.* **2013**, *125*, 6144 – 6148; b) T.-P. Fellinger, F. Hasché, P. Strasser, M. Antonietti, *J. Am. Chem. Soc.* **2012**, *134*, 4072 – 4075.
[21] a) S.-H. Yu, H. Cölfen, K. Tauer, M. Antonietti, *Nat. Mater.* **2005**, *4*, 51 – 55; b) H. Cölfen, M. Antonietti, *Angew. Chem. Int. Ed.* **2005**, *44*, 5576 – 5591; *Angew. Chem.* **2005**, *117*, 5714 – 5730.
[22] a) T. Ben, H. Ren, S. Ma, D. Cao, J. Lan, X. Jing, W. Wang, J. Xu, F. Deng, J. M. Simmons, S. Qiu, G. Zhu, *Angew. Chem. Int. Ed.* **2009**, *48*, 9457 – 9460; *Angew. Chem.* **2009**, *121*, 9621 – 9624; b) R. Vaidhyanathan, S. S. Iremonger, G. K. Shimizu, P. G. Boyd, S. Alavi, T. K. Woo, *Angew. Chem. Int. Ed.* **2012**, *51*, 1826 – 1829; *Angew. Chem.* **2012**, *124*, 1862 – 1865; c) A. M. Fracaroli, H. Furukawa, M. Suzuki, M. Dodd, S. Okajima, F. Gandara, J. A. Reimer, O. M. Yaghi, *J. Am. Chem. Soc.* **2014**, *136*, 8863 – 8866; d) D. H. Hong, M. P. Suh, *Chem. Eur. J.* **2014**, *20*, 426 – 434.
[23] a) J. Liang, Y. Jiao, M. Jaroniec, S. Z. Qiao, *Angew. Chem. Int. Ed.* **2012**, *51*, 11496 – 11500; *Angew. Chem.* **2012**, *124*, 11664 – 11668; b) Y. Zheng, Y. Jiao, L. Ge, M. Jaroniec, S. Z. Qiao, *Angew. Chem. Int. Ed.* **2013**, *52*, 3110 – 3116; *Angew. Chem.* **2013**, *125*, 3192 – 3198.
[24] M. Pimenta, G. Dresselhaus, M. S. Dresselhaus, L. Cancado, A. Jorio, R. Saito, *Phys. Chem. Chem. Phys.* **2007**, *9*, 1276 – 1290.
[25] J. Ren, M. Antonietti, T.-P. Fellinger, *Adv. Energy Mater.* **2014**, DOI: 10.1002/aenm.201401660.
[26] a) D. Eder, *Chem. Rev.* **2010**, *110*, 1348 – 1385; b) C. Zhang, M. Antonietti, T.-P. Fellinger, *Adv. Funct. Mater.* **2014**, *24*, 7655 – 7665.
[27] C. C. McCrory, S. Jung, J. C. Peters, T. F. Jaramillo, *J. Am. Chem. Soc.* **2013**, *135*, 16977 – 16987.

Received: December 4, 2014
Revised: January 21, 2015
Published online: March 4, 2015

